

Analysis and modelling of a novel process for extruding curved metal alloy profiles

Zhou, Wenbin; Lin, Jianguo; Dean, Trevor A.; Wang, Liliang

DOI:

[10.1016/j.ijmecsci.2018.02.028](https://doi.org/10.1016/j.ijmecsci.2018.02.028)

License:

Creative Commons: Attribution-NonCommercial-NoDerivs (CC BY-NC-ND)

Document Version

Peer reviewed version

Citation for published version (Harvard):

Zhou, W, Lin, J, Dean, TA & Wang, L 2018, 'Analysis and modelling of a novel process for extruding curved metal alloy profiles', *International Journal of Mechanical Sciences*, vol. 138-139, pp. 524-536.
<https://doi.org/10.1016/j.ijmecsci.2018.02.028>

[Link to publication on Research at Birmingham portal](#)

General rights

Unless a licence is specified above, all rights (including copyright and moral rights) in this document are retained by the authors and/or the copyright holders. The express permission of the copyright holder must be obtained for any use of this material other than for purposes permitted by law.

- Users may freely distribute the URL that is used to identify this publication.
- Users may download and/or print one copy of the publication from the University of Birmingham research portal for the purpose of private study or non-commercial research.
- User may use extracts from the document in line with the concept of 'fair dealing' under the Copyright, Designs and Patents Act 1988 (?)
- Users may not further distribute the material nor use it for the purposes of commercial gain.

Where a licence is displayed above, please note the terms and conditions of the licence govern your use of this document.

When citing, please reference the published version.

Take down policy

While the University of Birmingham exercises care and attention in making items available there are rare occasions when an item has been uploaded in error or has been deemed to be commercially or otherwise sensitive.

If you believe that this is the case for this document, please contact UBIRA@lists.bham.ac.uk providing details and we will remove access to the work immediately and investigate.

Accepted Manuscript

Analysis and modelling of a novel process for extruding curved metal alloy profiles

Wenbin Zhou , Jianguo Lin , Trevor A. Dean , Liliang Wang

PII: S0020-7403(17)32911-9
DOI: [10.1016/j.ijmecsci.2018.02.028](https://doi.org/10.1016/j.ijmecsci.2018.02.028)
Reference: MS 4188



To appear in: *International Journal of Mechanical Sciences*

Received date: 15 October 2017
Revised date: 10 February 2018
Accepted date: 12 February 2018

Please cite this article as: Wenbin Zhou , Jianguo Lin , Trevor A. Dean , Liliang Wang , Analysis and modelling of a novel process for extruding curved metal alloy profiles, *International Journal of Mechanical Sciences* (2018), doi: [10.1016/j.ijmecsci.2018.02.028](https://doi.org/10.1016/j.ijmecsci.2018.02.028)

This is a PDF file of an unedited manuscript that has been accepted for publication. As a service to our customers we are providing this early version of the manuscript. The manuscript will undergo copyediting, typesetting, and review of the resulting proof before it is published in its final form. Please note that during the production process errors may be discovered which could affect the content, and all legal disclaimers that apply to the journal pertain.

Highlights

- An analytical model for predicting metal profiles through a novel process, differential velocity sideways extrusion (DVSE), is proposed.
- The extrusion force, material flow velocity over the die orifice, extrudate curvature, and effective strain are determined.
- The theoretical results are verified with experimental and FEM results.

ACCEPTED MANUSCRIPT

Analysis and modelling of a novel process for extruding curved metal alloy profiles

Wenbin Zhou^a, Jianguo Lin^{a,*}, Trevor A. Dean^b, Liliang Wang^a

^a*Department of Mechanical Engineering, Imperial College London, London SW7 2AZ, UK*

^b*Department of Mechanical Engineering, University of Birmingham, Birmingham B15 2TT, UK*

Abstract

An analytical upper-bound-based model for predicting curvature of bent metal alloy profiles obtained through a novel extrusion process, differential velocity sideways extrusion (DVSE), previously proposed by the authors, has been first-time proposed. Finite element modelling and simulation and model material experiments, which were validated by extrusion of AA1050, have been performed to determine the geometry of the deformation zone and assess the accuracy of the analytical model. The extrusion force, curvature, and effective strain predicted by the analytical method agreed well with results from model material experiments and FE simulation. It was shown that the punch with a lower velocity experiences a lower extrusion force, which increases both with increase of its velocity and the extrusion ratio. The extrusion force on the faster punch with a constant velocity v_1 changes quite slightly with the increase of the velocity v_2 of the slower punch. Various values of curvature, which decrease with the increase of the punch velocity ratio v_2/v_1 and the decrease of the extrusion ratio, can be achieved through the DVSE process. DVSE is a novel process which leads to larger effective strain per pass than that in the equal channel angular extrusion (ECAE).

Keywords: Metal alloy profiles/sections; Bending; Curvature; Extrusion; Analytical analysis; Upper-bound method

* Corresponding author.

Email address: jianguo.lin@imperial.ac.uk (J. Lin).

Nomenclature

D_1	diameter of the billet
D_2	diameter of the extruded profile
dV	differential volume element of the plastic deformation zone (PDZ)
h	height of the dead metal zone (DMZ)
k_0, k_f	initial and final shear yield stresses of the material
\bar{k}	mean shear yield stress of the material
m	constant friction factor
F_1, F_2	extrusion forces of the upper and lower punches
F_{1u}, F_{2u}	upper bound of extrusion forces of the upper and lower punches
R_c	bending radius of the profile
S_0	cross-sectional area of the billet
S_3, S_4	cross-sectional areas of the related profile
S_f, S_v	areas of frictional and velocity discontinuity surfaces
Δv	amount of velocity discontinuity
v_1, v_2	extrusion velocities of the upper and lower punches
v_{1e}, v_{2e}	maximum and minimum material flow velocities across the die exit aperture
v_3, v_4	velocities at the volume (mass) centre of the related profile
\dot{W}_e, \dot{W}_i	external and internal power supplies
$\dot{W}_{S_f}, \dot{W}_{S_v}$	power dissipated on the frictional and velocity discontinuity surfaces
\bar{y}_3, \bar{y}_4	coordinates of the volume (mass) centre of the related profile

Greek symbols:

$\alpha, \beta, \theta, \varphi$	angles in the hodograph
γ	engineering shear strain
$\dot{\epsilon}_{ij}$	strain rate tensor
κ	bending curvature of the extruded profile
λ	extrusion ratio
ξ	eccentricity ratio

1. Introduction

Reducing the weight of metal components used in land, sea and air conveyances leads to reducing fuel consumption and therefore decreasing CO₂ emissions. Aluminium alloy profiles with various cross-sections are extensively used as construction elements in industrial manufacturing for the production of ultra-light structures, on account of their good combination of light weight and high strength. This is also because they can achieve the construction of complex, often aerodynamically shaped structures with little or no welding and cutting required, thus enhancing productivity [1-4]. Taking into account the demand for reduced aerodynamic resistance as well as improved aesthetics, the availability of precisely shaped curved aluminium alloy profiles with high performance properties is very attractive.

Conventional curved profile forming methods normally start with the manufacture of semi-finished straight profiles, by shape rolling or extrusion, followed by subsequent bending procedures such as; stretch bending, rotary draw bending, press bending, or roll bending (three-, four-, and six-roll processes). However, these production methods have the disadvantage of being two stages and also incurring springback and cross-sectional distortion in the second stage bending operation [5-10]. Recently, several novel integrated extrusion-bending methods have been proposed. The first one is curved profile extrusion (CPE) developed by Kleiner *et al.* [11,12] in which the hot metal billets are directly formed into continuous profiles/sections and bent simultaneously, thus greatly improving productivity. This process is based on the conventional straight extrusion process, with bending apparatus installed directly after the die exit to deflect the extruded profile to the prescribed curvature. Muller *et al.* [13,14] proposed a method in which a segmented regulating guiding device composed of serially placed bending discs is positioned at the die exit to bend the extruded straight profile. Since curvature is generated at the die exit where the material is still in the fully plastic state, this forming process produces profiles/sections with no springback, reduced residual stresses, and minimal cross-sectional distortion. Another way of achieving extrusion-bending integration is by utilising an inclined die, through which the material flow velocity distribution along the profile cross-section in the deformation zone can be adjusted. Shiraishi *et al.* [15-17] proposed a novel integrated extrusion-bending forming method for producing curved profiles, in which a billet is extruded through a die aperture inclined towards the central axis of the container at a predetermined angle. Experiments were carried out using plasticine as billets and it was found that by adjusting the inclination angle of the die aperture, the curvature of the extruded profile can be varied, and greater inclination angle leads to increased curvature.

The authors have proposed a new extrusion-bending process, differential velocity sideways extrusion (DVSE) [18,19]. The basic principle of this method is that profiles are bent in an

extrusion die orifice due to a velocity gradient across the cross-section of the extrudate. The velocity gradient is achieved by controlling the velocities of punches at each end of the billet work-piece. It has been shown that curvature of extrudate is dependent on the ratio of velocities of the two extrusion punches and the extrusion ratio. For a particular extrusion ratio, velocity ratio can be chosen to produce a particular curvature. An analytical model for predicting curvature of extrudate needs to be established for a deeper understanding and wider application of the DVSE forming method. The upper bound method has been extensively used to predict the forming force, optimise the forming process, analyse the deformation characteristic of the material in the extrusion of profiles, ring rolling and forging processes, and to determine and minimise the exit profile curvature in the extrusion process of non-symmetrical profiles [20-25], etc. It is considered to be suitable for analysing the complicated deformation characteristics of the DVSE process and to estimate the distribution of the profile curvature, both of which are influenced by several process parameters.

In this paper, an analytical model, based on the upper bound method, for estimating the distribution of extrusion force, curvature and effective strain of the extruded profile formed by DVSE, is developed. Finite element and physical models from practical experiments, have been used to assess the validity of the analytical model. The effects of punch velocity ratio, and extrusion ratio on extrusion force, curvature and effective strain of the formed profile, have been analysed in detail. The findings provide understanding needed for industrial exploitation of the DVSE process.

2. Theoretical model

2.1. Upper bound model

The upper bound model is formulated for a material extruded through circular orifices using the DVSE process. As shown as a section in **Fig. 1a**, consider a cylindrical container in which a billet, forced by a punch at each end, is extruded sideways through a circular die. The corresponding punch velocities and extrusion forces are v_1, F_1 and v_2, F_2 , respectively. The initial diameters of the billet and the container bore are both D_1 , the diameters of extruded profile and die exit aperture are both D_2 . For a rigid-plastic material, amongst all kinematically admissible velocity fields, the actual one minimizes the internal power required for material deformation:

$$\dot{W}_i = \int_V \sigma_{ij} \dot{\epsilon}_{ij} dV + \int_{S_v} k \Delta v dS_v + \int_{S_f} mk \Delta v dS_f - \int_{S_t} P_i v_i dS \quad (1)$$

where k is the current shear yield stress of the material, m is the constant friction factor, σ_{ij} and $\dot{\epsilon}_{ij}$ are the stress and strain rate tensors respectively, V is the volume of the plastic deformation zone, S_v and S_f are the areas of velocity discontinuity and frictional surfaces respectively, S_t is the area

where tension may occur, Δv is the amount of velocity discontinuity on the frictional and discontinuity surfaces, v_i and P_i are the velocity and traction applied on S_t , respectively.

Figure 1b shows a two dimensional deformation model considered on diametral planes of container and die. Based on the experimental and modelling results (see Section 4.1), the dead metal zone (DMZ) can be reasonably regarded as a triangle ΔAFC in this plane (the boundaries of the DMZ are simplified from the arc curves to straight lines, as the height BF of the dead zone is relatively small) whose central extension line BG divides the plastic deformation zone (PDZ) and the exit die channel into two parts; namely AB of length ξD_2 and CB of length $(1 - \xi)D_2$, respectively. Here the variable $\xi = g(v_2/v_1, \lambda)$ represents the effect of v_2/v_1 on the PDZ and DMZ for a given extrusion ratio λ . The material flowing into these two parts comes from both upper and lower regions of the container. The area of the DMZ and the position of line BG vary with values of v_2/v_1 and λ . When $v_2/v_1 = 1$, line BG is in the centre of the die exit channel. As v_2/v_1 decreases, it moves towards the side which has a lower extrusion velocity (v_2). As shown in **Fig. 1b**, the volume considered for analysis is divided into five regions. Regions I~IV are the PDZ in which the material undergoes plastic deformation, region V is the DMZ. A simple shear model is used here, thus the PDZ is considered as consisting of several single shear planes [26-27]. That is, the modes of deformation are composed of rigid blocks of material separated by the velocity discontinuity planes AE , EF , AF , CD , DF and CF .

Upper-bound solutions are obtained utilizing hodographs involving velocity discontinuities which are linear and occur only in the tangential direction along velocity discontinuity planes [26-27]. **Figure 1c** shows a solution utilizing a kinematically admissible hodograph. Before entering regions I and II, the material moves as a rigid body with the velocities v_1 and v_2 in the direction MO_1 and PO_2 until encountering the velocity discontinuities Δv_{AE} and Δv_{CD} at surfaces AE and CD , and are constrained to move in directions MN and PQ with velocities v_I and v_{II} respectively, at oblique angles β and θ to the die exit. Then, v_I and v_{II} further encounter velocity discontinuities Δv_{EF} and Δv_{DF} at surfaces EF and DF , and are forced to enter regions III and IV with velocities v_3 and v_4 in the hypothetical horizontal direction. It should be noted that v_3 and v_4 are the mean velocities of regions III and IV, since there is no velocity discontinuity between regions III and IV, and the velocity for the material flowing out of the die exit should be gradient where the upper side has the maximum velocity v_{1e} , the lower side has the minimum velocity v_{2e} and the boundary FG has the continuous velocity v_m . The die exit channel of the DVSE is sufficiently short [19] to ensure the differential velocities are not compromised by friction of the die bearing land. To calculate the area of the velocity discontinuity plane precisely and thus obtain accurate upper bound predictions, the

three-dimensional deformation model has been used, as shown in **Fig. 2**. From volume constancy, the material flow velocities v_3 and v_4 at the centres of volume (mass) of the profiles coming out of regions III, IV are found as

$$v_3 = \frac{S_0}{S_3} v_1 \quad (2)$$

$$v_4 = \frac{S_0}{S_4} v_2 \quad (3)$$

where

$$S_0 = \frac{\pi D_1^2}{4} \quad (4)$$

$$S_3 = \frac{D_2^2}{4} [\pi - \cos^{-1}(2\xi - 1)] + \sqrt{\xi - \xi^2} \left(\xi - \frac{1}{2} \right) D_2^2 \quad (5)$$

$$S_4 = \frac{D_2^2}{4} \cos^{-1}(2\xi - 1) - \sqrt{\xi - \xi^2} \left(\xi - \frac{1}{2} \right) D_2^2 \quad (6)$$

S_0 , S_3 and S_4 are the cross-sectional areas of the billet and the related profile, respectively. The detailed derivation can be seen in **Appendix A**.

The actual apparent extrusion ratio λ is defined by

$$\lambda = S_0 / (S_3 + S_4) = D_1^2 / D_2^2 \quad (7)$$

The first term in the right side of Eq. (1) is the internal power consumed in the PDZ. For a simple shear model, as the PDZ is considered as the single shear plane shape [26-27], only shear strain exists in the PDZ, then

$$\int_V \sigma_{ij} \dot{\epsilon}_{ij} dV = 2 \int_V \bar{k} \sqrt{\frac{1}{2} \dot{\epsilon}_{ij} \dot{\epsilon}_{ij}} dV = \int_V \bar{k} \dot{\gamma} dV \quad (8)$$

where \bar{k} is the mean shear yield strength of the material, $\dot{\gamma}$ is the equivalent engineering shear strain rate. Here we consider only cases where modes of deformation are composed of rigid blocks of material separated by planes of velocity discontinuity [26-27], i.e. $d\gamma = 0$, then $\int_V \bar{k} \dot{\gamma} dV = 0$. So, the first term in the right side of Eq. (1) can be neglected.

The second term in the right side of Eq. (1) can be separated into three parts ①–③ as follows. The detailed derivation can be seen in **Appendix B**.

Part ①–The power dissipated at the PDZ boundaries AE and EF when the material enters region I:

$$\dot{W}_{S_{v_1}} = \int_{S_{v_1}} \bar{k} \Delta v_1 dS_{v_1} \quad (9)$$

where $\Delta v_1 = \Delta v_{AE}, \Delta v_{EF}$ are velocity discontinuity variables, $S_{v_1} = S_{AE}, S_{EF}$ ($\hat{S}_{AE}, \hat{S}_{EF}$ in **Fig. 2**) are areas of velocity discontinuity planes. From the geometry and velocity relationships in **Figs. 1b-c**, Δv_{AE} and Δv_{EF} can be written as

$$\Delta v_{AE} = v_1 \cot \beta = v_1 \frac{h}{\xi D_2} \quad (10)$$

$$\Delta v_{EF} = \frac{(v_3 - \Delta v_{AE})}{\cos \alpha} = \frac{(v_3 - v_1 \frac{h}{\xi D_2})}{D_1 - h} \sqrt{(D_1 - h)^2 + \xi^2 D_2^2} \quad (11)$$

Here, variable $h = BF = f(v_2/v_1, \lambda)$ represents the height of the DMZ. We only consider the case $v_1 \geq v_2$, thus $0.5 \leq \xi < 1$. The related areas of velocity discontinuity planes are

$$S_{AE} = \hat{S}_{AE} = \frac{\pi D_1^2}{4} \quad (12)$$

$$S_{EF} = \hat{S}_{EF} = \frac{\pi D_1}{4} \sqrt{(D_1 - h)^2 + \xi^2 D_2^2} \quad (13)$$

where S_{EF} , as an approximation, is treated as an ellipse whose two axial lengths are D_1 and $\sqrt{(D_1 - h)^2 + \xi^2 D_2^2}$ (line EF in **Fig. 1b**).

Part ②—The power dissipated at PDZ boundaries CD and DF when the material enters region II:

$$\dot{W}_{S_{v_2}} = \int_{S_{v_2}} \bar{k} \Delta v_2 dS_{v_2} \quad (14)$$

where $\Delta v_2 = \Delta v_{CD}, \Delta v_{DF}$ are velocity discontinuity variables, $S_{v_2} = S_{CD}, S_{DF}$ ($\hat{S}_{CD}, \hat{S}_{DF}$ in **Fig. 2**) are areas of velocity discontinuity planes. Similarly, Δv_{CD} , Δv_{DF} and the related areas of velocity discontinuity planes are determined from **Figs. 1b-c** as

$$\Delta v_{CD} = v_2 \cot \theta = v_2 \frac{h}{(1 - \xi) D_2} \quad (15)$$

$$\Delta v_{DF} = \frac{(v_4 - \Delta v_{CD})}{\cos \varphi} = \frac{(v_4 - v_2 \frac{h}{(1 - \xi) D_2})}{D_1 - h} \sqrt{(D_1 - h)^2 + (1 - \xi)^2 D_2^2} \quad (16)$$

$$S_{CD} = \hat{S}_{CD} = \frac{\pi D_1^2}{4} \quad (17)$$

$$S_{DF} = \hat{S}_{DF} = \frac{\pi D_1}{4} \sqrt{(D_1 - h)^2 + (1 - \xi)^2 D_2^2} \quad (18)$$

Part ③–The power dissipated at the PDZ and DMZ boundaries AF and CF :

$$\dot{W}_{S_{v_3}} = \int_{S_{v_3}} \bar{k} \Delta v_3 dS_{v_3} \quad (19)$$

where $\Delta v_3 = \Delta v_{AF}, \Delta v_{CF}$ are velocity discontinuity variables, $S_{v_3} = S_{AF}, S_{CF}$ ($\hat{S}_{AFF'}$, $\hat{S}_{CF'}$ in **Fig. 2**) are areas of velocity discontinuity planes which are expressed as

$$\Delta v_{AF} = v_I = \frac{v_1}{\sin \beta} = \frac{v_1}{\xi D_2} \sqrt{h^2 + \xi^2 D_2^2} \quad (20)$$

$$\Delta v_{CF} = v_{II} = \frac{v_2}{\sin \theta} = \frac{v_2}{(1 - \xi) D_2} \sqrt{h^2 + (1 - \xi)^2 D_2^2} \quad (21)$$

$$S_{AF} = \hat{S}_{AFF'} = \frac{\pi}{2} \sqrt{D_1 h - h^2} \sqrt{h^2 + \xi^2 D_2^2} \quad (22)$$

$$S_{CF} = \hat{S}_{CF'} = \frac{\pi}{2} \sqrt{D_1 h - h^2} \sqrt{h^2 + (1 - \xi)^2 D_2^2} \quad (23)$$

The third term in the right side of Eq. (1) is the internal power dissipated by friction and can be broken into four parts ①–④. The detailed derivation can be seen in **Appendix B**.

Part ①–The power dissipated on friction between the material in regions I, II and die front and back walls:

$$\dot{W}_{S_{f_1}} = \int_{S_{f_1}} m \bar{k} \Delta v_1 dS_{f_1} \quad (24)$$

where $\Delta v_1 = \Delta v_{AF}, \Delta v_{CF}$ are velocity discontinuity variables obtained before in Eqs. (20)-(21), $S_{f_1} = S_{AEF}, S_{CDF}$ ($S_{AEF'}, S_{AEF''}, S_{CDF'}, S_{CDF''}$ in **Fig. 2**) are the areas of frictional surfaces which can be represented by

$$S_{AEF} = S_{AEF'} + S_{AEF''} = \frac{\pi \xi D_1 D_2}{2} \quad (25)$$

$$S_{CDF} = S_{CDF'} + S_{CDF''} = \frac{\pi (1 - \xi) D_1 D_2}{2} \quad (26)$$

Part ②–The power dissipated on friction between the material in regions III, IV and die front and back walls:

$$\dot{W}_{S_{f_2}} = \int_{S_{f_2}} mk_f \Delta v_2 dS_{f_2} \quad (27)$$

where k_f is the yield strength of the material after it has experienced plastic deformation, $\Delta v_2 = v_3, v_4$ are velocity discontinuity variables obtained before in Eqs. (2)-(3), $S_{f_2} = S_{EFH}, S_{DFH} (S_{EF'H'}, S_{EF''H''}, S_{DF'H'}, S_{DF''H''}$ in **Fig. 2**) are the areas of frictional surfaces which can be given by

$$\begin{aligned} S_{EFH} &= S_{EF'H'} + S_{EF''H''} \\ &= \frac{\xi D_1 D_2}{2} \left(\pi - \cos^{-1} \left(1 - \frac{2h}{D_1} \right) \right) - \frac{\pi D_1 D_2}{4} \left(\sin^{-1} \frac{D_2}{D_1} - (1 - \xi) \sin^{-1} \frac{2D_2 \sqrt{\xi - \xi^2}}{D_1} \right) \end{aligned} \quad (28)$$

$$\begin{aligned} S_{DFH} &= S_{DF'H'} + S_{DF''H''} \\ &= \frac{(1 - \xi) D_1 D_2}{2} \left(\pi - \cos^{-1} \left(1 - \frac{2h}{D_1} \right) \right) - \frac{\pi (1 - \xi) D_1 D_2}{4} \sin^{-1} \frac{2D_2 \sqrt{\xi - \xi^2}}{D_1} \end{aligned} \quad (29)$$

Part ③–The power dissipated on friction between the material in the die exit channel and die walls:

$$\dot{W}_{S_{f_3}} = \int_{S_{f_3}} mk_f \Delta v_3 dS_{f_3} \quad (30)$$

where $\Delta v_3 = v_3, v_4$ are related velocity discontinuity variables which are obtained before in Eqs. (2)-(3), $S_{f_3} = S_{EHG'E'}, S_{DHG'D'} (S_{EH'G'E'}, S_{EH''G''E'}, S_{DH'G'D'}, S_{DH''G''D'}$ in **Fig. 2**) are the areas of frictional surfaces which can be obtained as

$$\begin{aligned} S_{EHG'E'} &= S_{EH'G'E'} + S_{EH''G''E'} \\ &= \frac{\pi^2 D_2}{8} \left(D_1 - \sqrt{D_1^2 - D_2^2} \right) - \frac{\pi (1 - \xi) D_2}{4} \left(D_1 - \sqrt{D_1^2 - D_2^2 \sin^2(\cos^{-1}(2\xi - 1))} \right) \\ &\quad + D_2 l_3 (\pi - \cos^{-1}(2\xi - 1)) \end{aligned} \quad (31)$$

$$\begin{aligned} S_{DHG'D'} &= S_{DH'G'D'} + S_{DH''G''D'} \\ &= \frac{\pi (1 - \xi) D_2}{4} \left(D_1 - \sqrt{D_1^2 - D_2^2 \sin^2(\cos^{-1}(2\xi - 1))} \right) + D_2 l_3 \cos^{-1}(2\xi - 1) \end{aligned} \quad (32)$$

where l_3 is the length of the die bearing land.

Part ④–The power dissipated on friction between the material before it enters the PDZ region and die front and back walls is

$$\dot{W}_{S_{f4}} = \int_{S_{f4}} mk_0 \Delta v_4 dS_{f4} \quad (33)$$

where k_0 is the initial yield shear strength of the material, $\Delta v_4 = v_1, v_2$ are velocity discontinuities which are constants, $S_{f4} = \pi D_1 l_1, \pi D_1 l_2$ are the frictional surfaces of the entrance channel with respect to v_1, v_2 . Therefore,

$$\dot{W}_{S_{f4}} = \pi mk_0 D_1 (l_1 v_1 + l_2 v_2) \quad (34)$$

where l_1, l_2 are the transient billet lengths with velocities v_1, v_2 respectively, in the entrance channel.

In the DVSE process there is no external tension; so, the last term is equal to zero. Further, in every instance the last term in the right side of Eq. (1) is $\int_{S_t} P_i v_i dS = 0$. The total internal power consumed for the process \dot{W}_i can be calculated by summing the various components as

$$\dot{W}_i = \dot{W}_{S_v} + \dot{W}_{S_f} = \dot{W}_{S_{v1}} + \dot{W}_{S_{v2}} + \dot{W}_{S_{v3}} + \dot{W}_{S_{f1}} + \dot{W}_{S_{f2}} + \dot{W}_{S_{f3}} + \dot{W}_{S_{f4}} \quad (35)$$

For a given extrusion ratio λ and punch velocity ratio v_2/v_1 , parameter D_1/D_2 is fixed at any extrusion time, material coefficients (\bar{k}, k_0, k_f) and the dead zone height $h = f(v_2/v_1, \lambda)$ are also constants determined by the experiment, the total power in equation above is a function of the eccentricity ratio ξ . According to the upper-bound theorem, the actual solution for ξ is obtained when \dot{W}_i given in Eq. (35) reaches a minimum, i.e. differentiating the total power with respect to ξ and set the derivative equal to zero:

$$\frac{\partial \dot{W}_i}{\partial \xi} = 0 \quad (36)$$

The external supplied energy rate is

$$\dot{W}_e = \int_{S_c} P_i v_i dS = F_1 v_1 + F_2 v_2 \quad (37)$$

According to the upper bound theorem, the upper-bound solution is equal to or higher than the actually required force in metal forming process. That is, the total power consumed for the process is supplied by the upper bound of the external force, therefore we have

$$\dot{W}_{i,min} = \dot{W}_{eu} = F_{1u}v_1 + F_{2u}v_2 \quad (38)$$

This states that the external work done is equal to the internal energy consumed. Here, \dot{W}_{eu} , F_{1u} and F_{2u} are the upper bound solutions on \dot{W}_e , F_1 and F_2 , respectively. Minimising F_{1u} and F_{2u} with respect to parameter ξ determines the best upper bound on the value of F_1 and F_2 .

2.2. Determination of the extrudate bending curvature

Figure 3 illustrates the linear velocity distribution in the circular exit die, which is divided into two parts, namely ξD_2 and $(1 - \xi)D_2$. The extrudates flowing out of these two parts per unit time can be regarded as two ‘‘prisms’’ determined by the axial velocity v_z , whose centres of volume (mass) are O_3 and O_4 with axial material flow velocities v_3 and v_4 , respectively. These velocities v_3 and v_4 are defined in Eqs. (2)-(3). The y-coordinates of the centres of volume (mass) of the axial velocity prisms can be given by

$$\bar{y}_3 = \frac{\int_{S_3} y dV}{V_3} = \frac{\int_{S_3} y v_z dS_3}{S_3 v_3} \quad (39)$$

$$\bar{y}_4 = \frac{\int_{S_4} y dV}{V_4} = \frac{\int_{S_4} y v_z dS_4}{S_4 v_4} \quad (40)$$

where V_3, V_4 are the related volumes and dS_3, dS_4 are surface elements. Using geometrical relations between parameters of **Fig. 3**, the curvature radius and curvature of the exit profile have been obtained using the following equations:

$$R_c = \frac{\bar{y}_3 v_4 - \bar{y}_4 v_3}{v_3 - v_4} \quad (41)$$

$$\kappa = \frac{1}{R_c} \quad (42)$$

The detailed derivation can be seen in **Appendix C**.

3. Experimental and modelling methods

The model material plasticine and aluminium alloy 1050 (AA1050), annealed at 450°C for 1 hour, were used for the practical experiments. Uniaxial compression tests were first conducted on the aluminium alloy, for a 50% reduction in height on specimens of 12mm in height and 8 mm in diameter at room temperature (23°C), giving an initial shear yield value of 13MPa and a stress-strain relation as $\sigma = 145.5\varepsilon^{0.296}$, from which a final shear yield strength of 91MPa and a mean shear flow stress of 74MPa were obtained. The obtained true stress-strain data were also used in the

material model of the finite element analysis. **Figures 4a-b** show the designed and manufactured extrusion die set used for experiments [19]. The die set was split into two halves to facilitate easy removal of the extruded profiles. The container bore was 25.6mm in diameter and 150mm in height. Billets were 25.4mm in diameter and 130mm in length. The die orifices were circular, the length of the die bearing land was 2mm. The die set was made of AISI H13 hot work tool steel hardened and tempered to 50HRC. The assembled die set was positioned on a 2500kN Instron hydraulic press together with a double action mechanism which enabled the ratio of velocities of the punches to be varied; the velocity of the upper punch being that of the press. The specific illustration of the kinematics of the double-action mechanism can be seen in **Fig. 4c** [19], where the following relationship existed; $v_2/v_1 = v_{2p}/v_{1p} = LO/UO = LL'/UU'$.

To study deformation flow patterns, billets were cut into two halves lengthwise and square grids of 2mm×2mm were scribed on the diametral plane of one of the halves. The halves of aluminium billets were glued together and to reduce friction billets were coated with Omega-35 lubricant before being loaded into the container of the die set. The experimental method for model material plasticine was the same as that of our previous work [19]. The process was also modelled using the finite element software Deform-3D. A friction coefficient of 0.16 was used in the FE modelling, which was determined by comparing modelling results with extrusion tests of the AA1050 under a series of friction coefficients.

The parameters varied during the experiments and modelling were the diameter D_2 of the die orifice, and v_2 of the lower punch. The velocity of the upper punch was fixed at $v_1 = 1\text{mm/s}$, and v_2 had values, 0, 0.333mm/s, 0.5mm/s, 0.667mm/s and 1mm/s, to give velocity ratio v_2/v_1 values of, 0, 1/3, 1/2, 2/3, and 1. The limiting situation which gave the maximum curvature occurred when the velocity ratio $v_2/v_1 = 0$, namely the velocity of the lower punch was zero. This situation was of great significance since the test data was easily obtained from the actual extrusion process, and also it defined one forming limit of the profile curvature for a certain extrusion ratio. Therefore, the modelling was first performed to study the effect of the extrusion ratio for the case of cold extrusion of round bars at $v_2/v_1 = 0$, which could then be validated by the test data. Practical verification extrusion tests with AA1050, were carried out using the same process parameters as those adopted in the modelling.

4. Results and discussion

4.1. Validation of modelling results-curvatures, flow patterns, load-displacement curves

A comparison of curvatures and flow lines in AA1050 round bars and plasticine at velocity ratio $v_2/v_1 = 0$ and extrusion ratios $\lambda = 1.61, 2.87$ are shown in **Fig. 5**. The obtained curvature images

for the FE modelling are not separately shown here, which can be seen in Sections 4.3-4.4 in combination with the results of material flow velocity and effective strain distributions. It can be seen from **Fig. 5** that the extrudates are smoothly curved and apparently without defect or change in section diameter. A reasonably good agreement in curvature is achieved, though the curvature of AA1050 bar at higher extrusion ratio $\lambda = 2.87$ is slightly larger than those obtained by the plasticine experiment and FE modelling, the latter two are basically the same. This deviation is a result of the tool set expanding more at the higher extrusion pressures needed for aluminium, which affects the material flow at the die exit aperture. As can be seen in **Fig. 5** that burrs of the AA1050 extrudates occur especially for the case of $\lambda = 2.87$, due to the two halves of the die set parting slightly at high extrusion pressures. Grid distortions and dead metal zone (DMZ) are also similar for both aluminium and plasticine. Thus, the accuracy of the model material experiments is confirmed by extrusion tests of the AA1050. A dead metal zone, of near triangular shape, is situated against the container wall opposite the die exit orifice. Flow across sections of extrudates is not symmetrical and therefore curvature arises. The apex for the dead metal zone coincides with the dividing line of materials flowing into the extrudate, which is not on its centre-line but is closer to the side nearest the slower moving punch.

The load-displacement curves obtained from FE modelling and extrusion tests using AA1050 are compared in **Fig. 6**, for velocity ratio $v_2/v_1 = 0$ and extrusion ratios $\lambda = 1.61, 2.87$, respectively. Results from upper bound calculations are also plotted. It can be seen that a good agreement between the theoretical model, modelling and tests is achieved. Thus, the accuracy of the FE modelling is confirmed by the test data. It should be noticed that the extrusion forces at the initial stage obtained from the tests are lower than those predicted by FE modelling. As the strokes proceeds, the difference gradually decreases and modelled and experimental maximum extrusion forces at the stable stage become very close. This initial deviation is due to the fact that, in the experiments, the diameter of the billet is slightly smaller than that of the extrusion container, thus upsetting occurs first. However, in FE modelling the billet and the extrusion container are of the same diameter. Also it can be seen that the extrusion forces predicted by the upper bound method are greater than both those from FE modelling and practical tests, which is to be expected from upper bound theory. The gradual decrease in load with stroke is because of decreased frictional surface area in the container as extrusion proceeds.

4.2. Comparison of theoretical and experimental extrusion force

The theoretical and numerical extrusion force vs. velocity ratio curves are compared in **Fig. 7**, for velocity ratio $v_2/v_1 = 0 \sim 1$ and extrusion ratios $\lambda = 1.61, 2.87$, respectively. The stroke value

where the extrusion force F_1 for the upper punch reaches peak value, was firstly obtained from FE modelling, then the theoretical extrusion force was calculated using this stroke. The extrusion force F_2 for the lower punch at this extrusion moment was also extracted. These results show a good agreement between the theoretical model, FE modelling and experiments, though the theoretical values are always slightly greater. As shown in **Fig. 7**, extrusion forces of both upper and lower punches increase as the increase of the extrusion ratio and velocity ratio. However, the increase of the extrusion force of the upper punch with a constant velocity v_1 is much slower than that of the lower punch, especially when $v_2/v_1 < 1/3$. The upper punch has a bigger extrusion force than that of the lower punch when $v_2/v_1 < 1$, since the extrusion force F_2 for the lower punch has not reached the maximum value yet when F_1 reaches peak value. The difference in the extrusion force gradually decreases as v_2/v_1 (i.e. v_2) increases, and the two extrusion forces become equal when the velocity ratio is 1.

4.3. Comparison of theoretical and experimental extrudate curvature

The material flow velocity distribution at the die exit obtained from FE modelling is shown in **Fig. 8**. It is compared with that obtained from theoretical analysis, as illustrated in **Fig. 9a**. The bending curvature obtained from FE modelling and plasticine extrusion experiments, is shown in **Fig. 9b**. These were estimated by fitting the resulting images with perfect circles of the same scale. After getting the radius R_c of the circle, the curvature can be obtained as $1/R_c$. The curvature predicted from the theoretical model is also plotted for comparison. It is clearly seen from **Figs. 9a-b** that a good agreement on predicted velocities between the theoretical model and FE modelling exists. Greater extrusion ratio λ and smaller velocity ratio v_2/v_1 leads to an increased velocity gradient at the die exit and thus greater curvature, although the theoretically predicted curvature is slightly greater than that from FE modelling and plasticine extrusion experiments due to the predicted velocity gradient being slightly greater, especially when $v_2/v_1 < 1/3$. The curvature difference can also be seen from **Fig. 8** that the radius of the curvature related circle which is circled by the velocity gradient lines is slightly smaller than that of the bending profile itself for all cases of $v_2/v_1 < 1$. This curvature difference gradually decreases as the extrusion ratio λ decreases and the velocity ratio v_2/v_1 increases, which is in accordance with that shown in **Fig. 9b**.

4.4. Comparison of theoretical and experimental effective strain

As discussed before, the cross-section of material in the die exit aperture can be divided into two parts and the material flowing into these two parts comes from the corresponding two extrusion punches. The profile is therefore regarded as being composed of two parts; the inside bending part closer to the slower punch and the outside bending part closer to the faster punch. The flow of

material into the die exit aperture has a similarity to that experienced by material in the non-equal channel angular extrusion (N-EACE) process, depending on the eccentricity ratio ξ . To calculate the eccentricity ratio ξ , the dead zone height $h = f(v_2/v_1, \lambda)$ was firstly obtained from plasticine extrusion experiments and FE modelling as shown in **Fig. 10a**. It can be seen that h decreases nonlinearly with increase of punch velocity ratio v_2/v_1 and extrusion ratio λ , and the following relation is obtained by curve fitting:

$$h = f\left(\frac{v_2}{v_1}, \lambda\right) = \left(0.264\left(1 - \frac{v_2}{v_1}\right)^{2.394} + 0.5\right)^3 \lambda^{-1.5} D_1 \quad (43)$$

Substituting Eq. (43) into Eq. (36), the eccentricity ratio variable ξ can be obtained as shown in **Fig. 10b**. The results obtained from plasticine extrusion experiments and FE modelling are also illustrated for comparison. It can be seen that a reasonably good agreement is achieved though there are some small differences when ξ is close to 0.5, considering the error is inevitably produced since ξ from experiments and FE modelling is manually measured.

For a N-ECAE die without rounding of the corners at the intersection of the channels, the simple shear model gives the value of shear strain in one pass as [27]

$$\gamma = \cot \alpha_1 + \cot \alpha_2 \quad (44)$$

where α_1 and α_2 are the angles of the intersection plane with the entry and exit channels, respectively. For a 90° NECAE die, the value of effective strain can be calculated from Eq. (44) as

$$\varepsilon = \gamma/\sqrt{3} = (D_i/D_e + D_e/D_i)/\sqrt{3} \quad (45)$$

where D_i and D_e are diameters of the entry channel and the exit channel, respectively. Here, $D_i = D_1 = 25.6\text{mm}$ is the same for all velocity ratios and extrusion ratios, however, as discussed before the die exit can be divided into two parts, which vary with the variation of the velocity ratio v_2/v_1 for a given extrusion ratio λ . Only the effective strain of outside bending part of the profile is calculated here, thus $D_e = \xi D_2$, where ξ is shown in **Fig. 10b**. Since bending occurs with shear deformation, to minimise the effect of bending on element deformation, only the effective strain in the neutral plane ($\sim 1/2 \xi D_2$) of the outside bending part of the profile is extracted from FE modelling. The areas above and below the neutral plane have almost equal effective strain which is greater than that of the neutral plane, as shown in **Fig. 11**. The comparison of the effective strain is shown in **Fig. 12**. It can be seen that the effective strain obtained from FE modelling is slightly greater than that of theory and plasticine extrusion experiments, though the bending curvature obtained from FE modelling is slightly lower. This may be due to the fact that Eq. (45) is essentially obtained from the simple shear model where only shear strain is considered during the deformation

zone of ECAE or N-ECAE, also it is actually more applicable to the plane strain case, however the DVSE considered here is a three dimensional extrusion process, and bending is accompanied with extrusion as well [19]. The effective strain in per pass of a 90 degree ECAE die is $2/\sqrt{3} = 1.15$ given by the simple shear model [28], thus DVSE results in greater effective strain level than that per pass in ECAE.

5. Conclusions

An analytical model based on the upper bound theory has been first-time proposed to analyse a novel extrusion process, differential velocity sideways extrusion (DVSE), previously proposed by the authors for forming curved profiles. The extrusion force, extrudate curvature, and effective strain predicted by the analytical model were in good agreement with modelling and experimental results, it was found that the lower punch produces a lower extrusion force due to its lower velocity v_2 , but increases with increase of its velocity, particularly at low values of velocity ratio, less than $1/3$. The force on the faster upper punch with a constant velocity v_1 changes only slightly with the increase of the velocity v_2 . Bending curvature of the extruded profiles can be adjusted in the DVSE process; they decrease with the decrease of extrusion ratio and increase of velocity ratio v_2/v_1 . DVSE is a novel process which results in greater effective strain level than that per pass in the equal channel angular extrusion (ECAE).

Acknowledgement

The financial support from the President's PhD Scholarship of Imperial College London is greatly appreciated.

Appendix A

Referring to **Fig. A1**, the following relationships can be obtained as

$$G'G'' = 2D_2\sqrt{\xi - \xi^2} \quad (\text{A1})$$

$$S_{\Delta OG'G''} = \sqrt{\xi - \xi^2} \left(\xi - \frac{1}{2} \right) D_2^2 \quad (\text{A2})$$

$$\theta = \cos^{-1}(2\xi - 1) \quad (\text{A3})$$

$$\begin{aligned} \widehat{S}_{2\theta \square} &= S_{OG'D'G''} = \frac{1}{4}\theta D_2^2 \\ &= \frac{D_2^2}{4} \cos^{-1}(2\xi - 1) \end{aligned} \quad (\text{A4})$$

$$S_4 = \widehat{S}_{2\Theta} - S_{\Delta OG'G''} = \frac{D_2^2}{4} \cos^{-1}(2\xi - 1) - \sqrt{\xi - \xi^2} \left(\xi - \frac{1}{2} \right) D_2^2 \quad (\text{A5})$$

$$S_3 = \frac{\pi D_2^2}{4} - S_4 = \frac{D_2^2}{4} [\pi - \cos^{-1}(2\xi - 1)] + \sqrt{\xi - \xi^2} \left(\xi - \frac{1}{2} \right) D_2^2 \quad (\text{A6})$$

Appendix B

The velocity discontinuity planes between the PDZ and DMZ are established in **Fig. B1** as $AF'F''$ and $CF'F''$. The area of $AF'F''$ is given by

$$F'F'' = 2\sqrt{D_1 h - h^2} \quad (\text{B1})$$

$$AF = \sqrt{h^2 + \xi^2 D_2^2} \quad (\text{B2})$$

$$CF = \sqrt{h^2 + (1 - \xi)^2 D_2^2} \quad (\text{B3})$$

$$\begin{aligned} \widehat{S}_{AF'F''} &= \frac{\pi}{4} F'F'' \cdot AF \\ &= \frac{\pi}{2} \sqrt{D_1 h - h^2} \sqrt{h^2 + \xi^2 D_2^2} \end{aligned} \quad (\text{B4})$$

Similarly, the area of $CF'F''$ is given by

$$\begin{aligned} \widehat{S}_{CF'F''} &= \frac{\pi}{4} F'F'' \cdot CF \\ &= \frac{\pi}{2} \sqrt{D_1 h - h^2} \sqrt{h^2 + (1 - \xi)^2 D_2^2} \end{aligned} \quad (\text{B5})$$

The frictional surfaces between the PDZ and die front and back walls are established in **Fig. 2** as AEF' and AEF'' . The areas of AEF' and AEF'' are given by

$$S_{AEF'} = S_{AEF''} = \frac{1}{2} \frac{\pi D_1}{2} \xi D_2 = \frac{\pi \xi D_1 D_2}{4} \quad (\text{B6})$$

Similarly, the areas of CDF' and CDF'' can be given by

$$S_{CDF'} = S_{CDF''} = \frac{1}{2} \frac{\pi D_1}{2} (1 - \xi) D_2 = \frac{\pi (1 - \xi) D_1 D_2}{4} \quad (\text{B7})$$

The frictional surfaces between the regions III, IV and die front and back walls are established in **Fig. 2** as $EF'H'$, $EF''H''$ and $DF'H'$, $DF''H''$. The surface $EH'DH''E$ on the cylinder of diameter D_1 is shown in **Fig. B2**, which is surrounded by the intersecting line of the two cylinders. Any point on the intersecting line EKD can be expressed in the O_1 - x - y coordinate system as

$$x = \frac{D_1}{2} \phi, \quad y = \sqrt{\left(\frac{D_2}{2}\right)^2 - \left(\frac{D_1}{2}\right)^2 \sin^2 \phi} \quad (\text{B8})$$

where point K and H' can be obtained by substituting $\phi = \phi_1$, and $\phi = \phi_2$, respectively:

$$\phi_1 = \sin^{-1} \frac{D_2}{D_1}, \quad \phi_2 = \sin^{-1} \frac{G'G''}{D_1} = \sin^{-1} \frac{2D_2\sqrt{\xi - \xi^2}}{D_1} \quad (\text{B9})$$

A surface element on the $EH'DH''E$ is given by

$$dS = \frac{D_1}{2} \sqrt{\left(\frac{D_2}{2}\right)^2 - \left(\frac{D_1}{2}\right)^2 \sin^2 \phi} d\phi \quad (\text{B10})$$

The areas of $EH'DH''E$, $DH'H''$ and $EH'H'$ are given by

$$S_{EH'DH''E} = 4 \int_0^{\phi_1} dS = 4 \int_0^{\sin^{-1} \frac{D_2}{D_1}} \frac{D_1}{2} \sqrt{\left(\frac{D_2}{2}\right)^2 - \left(\frac{D_1}{2}\right)^2 \sin^2 \phi} d\phi = \frac{\pi D_1 D_2}{4} \sin^{-1} \frac{D_2}{D_1} \quad (\text{B11})$$

$$S_{DH'H''} = 2 \left(\int_0^{\phi_2} dS - \frac{D_1}{2} \beta \sqrt{\left(\frac{D_2}{2}\right)^2 - \left(\frac{D_1}{2}\right)^2 \sin^2 \beta} \right) = \frac{\pi(1-\xi)D_1 D_2}{4} \sin^{-1} \frac{2D_2\sqrt{\xi - \xi^2}}{D_1} \quad (\text{B12})$$

$$S_{EH'H''} = S_{EH'DH''E} - S_{DH'H''} = \frac{\pi D_1 D_2}{4} \left(\sin^{-1} \frac{D_2}{D_1} - (1-\xi) \sin^{-1} \frac{2D_2\sqrt{\xi - \xi^2}}{D_1} \right) \quad (\text{B13})$$

$\hat{l}_{F'F''}$ is obtained from **Fig. B1** as

$$\Psi = \cos^{-1} \left(1 - \frac{2h}{D_1} \right) \quad (\text{B14})$$

$$\hat{l}_{F'F''} = (\pi - \Psi)D_1 = \left(\pi - \cos^{-1} \left(1 - \frac{2h}{D_1} \right) \right) D_1 \quad (\text{B15})$$

The areas of $EF'H'$ and $EF''H''$ are given by

$$S_{\Delta EF'F''} = \frac{1}{2} \hat{l}_{F'F''} \cdot \xi D_2 = \frac{\xi D_1 D_2}{2} \left(\pi - \cos^{-1} \left(1 - \frac{2h}{D_1} \right) \right) \quad (\text{B16})$$

$$\begin{aligned}
S_{EF'H'} = S_{EF''H''} &= \frac{1}{2}(S_{\Delta EF'F''} - S_{EH'H''}) \\
&= \frac{\xi D_1 D_2}{4} \left(\pi - \cos^{-1} \left(1 - \frac{2h}{D_1} \right) \right) - \frac{\pi D_1 D_2}{8} \left(\sin^{-1} \frac{D_2}{D_1} - (1 - \xi) \sin^{-1} \frac{2D_2 \sqrt{\xi - \xi^2}}{D_1} \right)
\end{aligned} \tag{B17}$$

Similarly, the areas of $DF'H'$ and $DF''H''$ can be given by

$$\begin{aligned}
S_{DF'H'} = S_{DF''H''} &= \frac{1}{2}(S_{\Delta DF'F''} - S_{DH'H''}) \\
&= \frac{(1 - \xi) D_1 D_2}{4} \left(\pi - \cos^{-1} \left(1 - \frac{2h}{D_1} \right) \right) - \frac{\pi(1 - \xi) D_1 D_2}{8} \sin^{-1} \frac{2D_2 \sqrt{\xi - \xi^2}}{D_1}
\end{aligned} \tag{B18}$$

The surface $EH'DJ'E$ on the cylinder of diameter D_2 is shown in **Fig. B3**, which is surrounded by the intersecting line of the two cylinders. Any point on the intersecting line $EH'D$ can be expressed in the D - x - y coordinate system as

$$x = \frac{D_2}{2} \phi, \quad y = \sqrt{\left(\frac{D_1}{2}\right)^2 - \left(\frac{D_2}{2}\right)^2 \sin^2 \phi} \tag{B19}$$

where point H' can be obtained by substituting $\phi = \theta = \cos^{-1}(2\xi - 1)$ (Eq. (A3).) into Eq. (B19).

A surface element on the $EH'DJ'E$ is given by

$$dS = \frac{D_2}{2} \left(\frac{D_1}{2} - \sqrt{\left(\frac{D_1}{2}\right)^2 - \left(\frac{D_2}{2}\right)^2 \sin^2 \phi} \right) d\phi \tag{B20}$$

The areas of $EH'G'E'$ and $DH'G'D'$ are given by

$$\begin{aligned}
S_{EH'DJ'E} = S_{EH''DJ''E} &= 2 \int_0^{\frac{\pi}{2}} dS = 2 \int_0^{\frac{\pi}{2}} \frac{D_2}{2} \left(\frac{D_1}{2} - \sqrt{\left(\frac{D_1}{2}\right)^2 - \left(\frac{D_2}{2}\right)^2 \sin^2 \phi} \right) d\phi \\
&\doteq \frac{\pi^2 D_2}{16} \left(D_1 - \sqrt{D_1^2 - D_2^2} \right)
\end{aligned} \tag{B21}$$

$$\begin{aligned}
S_{DH'J'} = S_{DH''J''} &= \int_0^{\theta} dS = \int_0^{\cos^{-1}(2\xi-1)} \frac{D_2}{2} \left(\frac{D_1}{2} - \sqrt{\left(\frac{D_1}{2}\right)^2 - \left(\frac{D_2}{2}\right)^2 \sin^2 \phi} \right) d\phi \\
&\doteq \frac{\pi(1 - \xi) D_2}{8} \left(D_1 - \sqrt{D_1^2 - D_2^2 \sin^2(\cos^{-1}(2\xi - 1))} \right)
\end{aligned} \tag{B22}$$

$$\begin{aligned}
S_{EH'J'} &= S_{EH''J''} = S_{EH'DJ'E} - S_{DH'J'} \\
&= \frac{\pi^2 D_2}{16} \left(D_1 - \sqrt{D_1^2 - D_2^2} \right) - \frac{\pi(1-\xi)D_2}{8} \left(D_1 - \sqrt{D_1^2 - D_2^2 \sin^2(\cos^{-1}(2\xi - 1))} \right)
\end{aligned} \tag{B23}$$

$$\begin{aligned}
S_{EH'G'E} &= S_{EH''G''E} = S_{EH'J'} + S_{EJ'G'E} \\
&= \frac{\pi^2 D_2}{16} \left(D_1 - \sqrt{D_1^2 - D_2^2} \right) - \frac{\pi(1-\xi)D_2}{8} \left(D_1 - \sqrt{D_1^2 - D_2^2 \sin^2(\cos^{-1}(2\xi - 1))} \right) \\
&\quad + \frac{D_2 l_3}{2} (\pi - \cos^{-1}(2\xi - 1))
\end{aligned} \tag{B24}$$

$$\begin{aligned}
S_{DH'G'D'} &= S_{DH''G''D'} = S_{DH'J'} + S_{DJ'G'D'} \\
&= \frac{\pi(1-\xi)D_2}{8} \left(D_1 - \sqrt{D_1^2 - D_2^2 \sin^2(\cos^{-1}(2\xi - 1))} \right) + \frac{D_2 l_3}{2} \cos^{-1}(2\xi - 1)
\end{aligned} \tag{B25}$$

Appendix C

Figure 3 shows the linear velocity distribution in a circular zone. In this figure, D_2 is the diameter of the zone and v_3 and v_4 are the axial velocities at coordinates \bar{y}_3 and \bar{y}_4 , respectively. R_c is the radius of the exit profile curvature. Assume after a finite time element Δt , the extrudates at points O_3, O_4 move Δd_3 and Δd_4 , due to $\Delta d_3 > \Delta d_4$ the exit profile will not come out straight and will have a bending angle $\Delta\theta_c$, the following kinematic relations exist:

$$\Delta d_3 = v_3 \Delta t \tag{C1}$$

$$\Delta d_4 = v_4 \Delta t \tag{C2}$$

The related geometrical relations are

$$\Delta d_3 = \Delta\theta_c (R_c + \bar{y}_3) \tag{C3}$$

$$\Delta d_4 = \Delta\theta_c (R_c + \bar{y}_4) \tag{C4}$$

Substituting Eqs. (C3)-(C4) into Eqs. (C1)-(C2), the curvature radius of the exit profile is given by

$$R_c = \frac{\bar{y}_3 v_4 - \bar{y}_4 v_3}{v_3 - v_4} \tag{C5}$$

The y-coordinates of the centres of volume (mass) of the axial velocity prisms can be expressed as

$$\bar{y}_3 = \frac{\int_{S_3} y dV}{V_3} = \frac{\int_{S_3} y v_z dS_3}{S_3 v_3} \quad (C6)$$

$$\bar{y}_4 = \frac{\int_{S_4} y dV}{V_4} = \frac{\int_{S_4} y v_z dS_4}{S_4 v_4} \quad (C7)$$

According to the law of conservation of mass:

$$v_o = \frac{S_0}{S_3 + S_4} (v_1 + v_2) = \frac{D_1^2}{D_2^2} (v_1 + v_2) \quad (C8)$$

v_z can be expressed in terms of \bar{y}_3 as

$$v_z = \frac{v_3 - v_o}{\bar{y}_3} y + v_o \quad (C9)$$

Substituting Eqs. (C8)-(C9) into Eq. (C6), \bar{y}_3 is implicitly expressed as

$$\begin{aligned} \bar{y}_3 &= \frac{\int_{S_3} y v_z dS_3}{S_3 v_3} = \frac{1}{S_3 v_3} \int_{-(\xi - \frac{1}{2})D_2}^{\frac{D_2}{2}} 2y \sqrt{\left(\frac{D_2}{2}\right)^2 - y^2} \left(\frac{v_3 - v_o}{\bar{y}_3} y + v_o\right) dy \\ &= \frac{2(v_3 - v_o)}{\bar{y}_3 S_3 v_3} \left\{ \frac{-(\xi - \frac{1}{2})D_2}{4} \left[\left(\frac{D_2}{2}\right)^2 - \left(\xi - \frac{1}{2}\right)^2 D_2^2 \right]^{\frac{3}{2}} \right. \\ &\quad \left. + \frac{D_2^2}{32} \left[\left(\xi - \frac{1}{2}\right) D_2 \left[\left(\frac{D_2}{2}\right)^2 - \left(\xi - \frac{1}{2}\right)^2 D_2^2 \right]^{\frac{1}{2}} + \left(\frac{D_2}{2}\right)^2 \left(\frac{\pi}{2} - \sin^{-1}(1 - 2\xi)\right) \right] \right\} \\ &\quad + \frac{2v_o}{3S_3 v_3} \left[\left(\frac{D_2}{2}\right)^2 - \left(\xi - \frac{1}{2}\right)^2 D_2^2 \right]^{\frac{3}{2}} \end{aligned} \quad (C10)$$

Thus \bar{y}_3 can be obtained by numerically solving the following equation:

$$\bar{y}_3^2 - g_1(\xi)\bar{y}_3 - g_2(\xi) = 0 \quad (C11)$$

where $\bar{y}_3 > 0$ is the positive root, $g_1(\xi), g_2(\xi)$ are only functions of ξ which are expressed as

$$g_1(\xi) = \frac{2v_o}{3S_3 v_3} \left[\left(\frac{D_2}{2}\right)^2 - \left(\xi - \frac{1}{2}\right)^2 D_2^2 \right]^{\frac{3}{2}} \quad (C12)$$

$$g_2(\xi) = \frac{2(v_3 - v_o)}{S_3 v_3} \left\{ \frac{-\left(\xi - \frac{1}{2}\right) D_2 \left[\left(\frac{D_2}{2}\right)^2 - \left(\xi - \frac{1}{2}\right)^2 D_2^2 \right]^{\frac{3}{2}}}{4} + \frac{D_2^2}{32} \left[\left(\xi - \frac{1}{2}\right) D_2 \left[\left(\frac{D_2}{2}\right)^2 - \left(\xi - \frac{1}{2}\right)^2 D_2^2 \right]^{\frac{1}{2}} + \left(\frac{D_2}{2}\right)^2 \left(\frac{\pi}{2} - \sin^{-1}(1 - 2\xi) \right) \right] \right\} \quad (C13)$$

\bar{y}_4 can be obtained similarly. Then v_{1e}, v_{2e} can be given by substituting $y = \pm 0.5D_2$ into Eq. (C9).

References

- [1] Kleiner M, Chatti S, Klaus A. Metal forming techniques for lightweight construction. *J Mater Process Technol* 2006;177:2-7.
- [2] Schneider M, Koehler G, Becker D, Selvaggio A, Tekkaya AE, Munzinger C, Schulze V, Kleiner M. Towards the flexible and near-net-shape production of three dimensionally curved extrusion profiles. *Prod Eng Res Devel* 2010;4:561-9.
- [3] Hermes M, Staupendahl D, Becker C, Tekkaya AE. Innovative machine concepts for 3D bending of tubes and profiles. *Key Eng Mater* 2011;473:37-42.
- [4] Tekkaya AE, Khalifa NB, Grzancic G, Hölker R. Forming of lightweight metal components: Need for new technologies. *Procedia Eng* 2014;81:28-37.
- [5] Paulsen F, Welo T. Cross-sectional deformations of square hollow sections in bending: part II-analytical models. *Int J Mech Sci* 2001;43:131-52.
- [6] Clausen AH, Hopperstad OS, Langseth M. Sensitivity of model parameters in stretch bending of aluminum extrusions. *Int J Mech Sci* 2001;43:427-53.
- [7] Miller JE, Kyriakides S, Bastard AH. On bend-stretch forming of aluminum extruded tubes-I: Experiments. *Int J Mech Sci* 2001;43:1283-317.
- [8] Miller JE, Kyriakides S, Bastard AH. On bend-stretch forming of aluminum extruded tubes-II: Analysis. *Int J Mech Sci* 2001;43:1319-38.
- [9] Zhao J, Zhai RX, Qian ZP, Ma R. A study on springback of profile plane stretch-bending in the loading method of pretension and moment. *Int J Mech Sci* 2013;75:45-54.
- [10] Liao J, Xue X, Lee MG, Barlat F, Gracio J. On twist springback prediction of asymmetric tube in rotary draw bending with different constitutive models. *Int J Mech Sci* 2014;89:311-22.
- [11] Hermes M, Kleiner M. Method and device for profile bending. In: European Patent EP2144720B1; 2008.
- [12] Selvaggio A, Becker D, Klaus A, Arendes D, Kleiner M. Curved Profile Extrusion. In: Tekkaya AE, Homberg W, Brosius A, editors. 60 Excellent Inventions in Metal Forming. Berlin: Springer Verlag; 2015. p. 287-92.
- [13] Müller KB. Bending of extruded profiles during extrusion process. *Mater Forum* 2004;28:264-9.

- [14] Müller KB. Bending of extruded profiles during extrusion process. *Int J Mach Tools Manufact* 2006;46:1238-42.
- [15] Shiraishi M, Nikawa M, Goto Y. An investigation of the curvature of bars and tubes extruded through inclined dies. *Int J Mach Tools Manufact* 2003;43:1571-8.
- [16] Nikawa M, Shiraishi M, Miyajima Y, Horibe H, Goto Y. Production of shaped tubes with various curvatures using extrusion process through inclined die aperture. *J Jpn Soc Technol Plast* 2002;43: 654-6.
- [17] Takahashi Y, Kihara S, Yamaji K, Shiraishi M. Effects of die dimensions for curvature extrusion of curved rectangular bars. *J Mater Process Technol* 2015;56:844-9.
- [18] Zhou WB, Lin JG, Dean TA, Wang LL. A novel application of sideways extrusion to produce curved aluminium profiles: Feasibility study. *Procedia Eng* 2017;207:2304-9.
- [19] Zhou WB, Lin JG, Dean TA, Wang LL. Feasibility studies of a novel extrusion process for curved profiles: Experiments and modelling, *Int J Mach Tools Manufact* 2018;126:27-43.
- [20] Celik KF, Chitkara NR. Application of an upper bound method to off-centric extrusion of square sections, analysis and experiments. *Int J Mech Sci* 2000;42:321-45.
- [21] Ajiboye JS, Adeyemi MB. Upper bound analysis for extrusion at various die land lengths and shaped profiles. *Int J Mech Sci* 2007;49:335-51.
- [22] Rastegar M, Assempour A, Ghazanfari A. Determination of geometrical parameters of the dead metal zone and exit Curvature profile in the extrusion process of non-symmetrical flat dies. *SAE Technical Paper No. 2012-01-0052*; 2012.
- [23] Ghassemali E, Tan MJ, Jarfors AE, Lim SCV. Optimization of axisymmetric open-die micro-forging/extrusion processes: An upper bound approach. *Int J Mech Sci* 2013;71:58-67.
- [24] Parvizi A, Abrinia K. A two dimensional upper bound analysis of the ring rolling process with experimental and FEM verifications. *Int J Mech Sci* 2014;79:176-81.
- [25] Wu YJ, Dong XH, Yu Q. Upper bound analysis of axial metal flow inhomogeneity in radial forging process. *Int J Mech Sci* 2015;93:102-10.
- [26] Sheppard T. *Extrusion of Aluminium Alloys*. Dordrecht: Kluwer Academic Press; 1999.
- [27] Lee DN. An upper-bound solution of channel angular deformation. *Scr Mater* 2000;43:115-8.
- [28] Tóth LS, Massion RA, Germain L, Baik SC, Suwas S. Analysis of texture evolution in equal channel angular extrusion of copper using a new flow field. *Acta Mater* 2004; 52:1885-98.

Figures and Tables

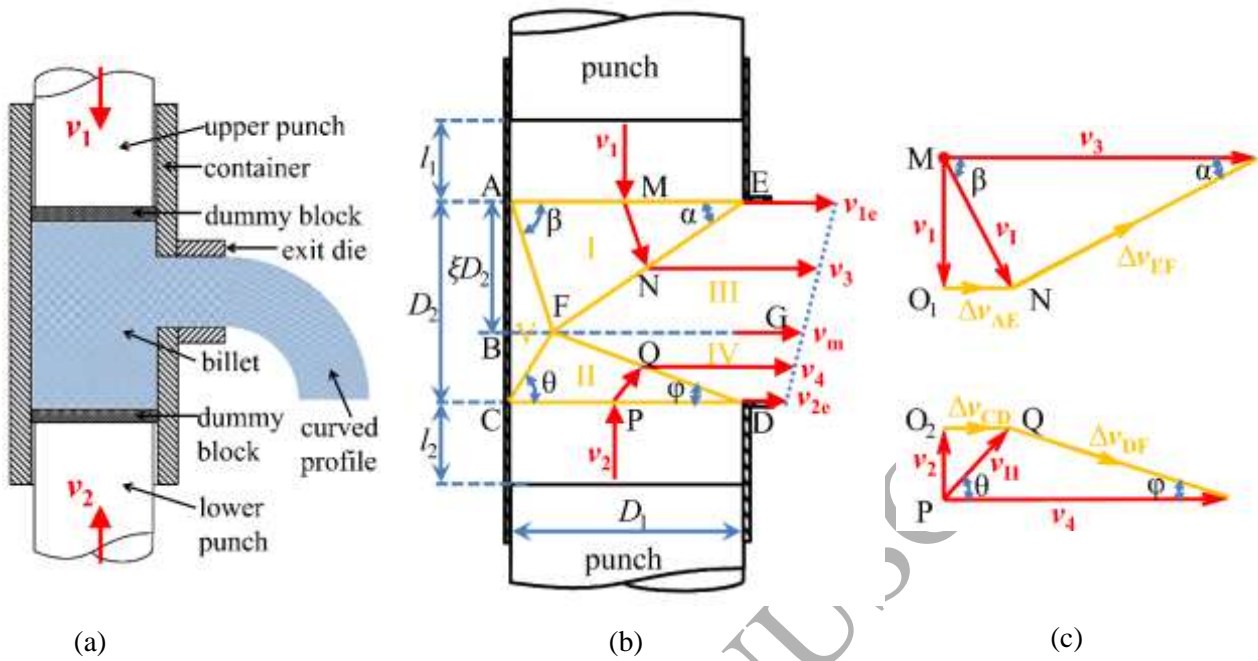


Fig. 1. (a) Schematic of the differential velocity sideways extrusion (DVSE) process, (b) two dimensional deformation model, (c) the related hodograph.

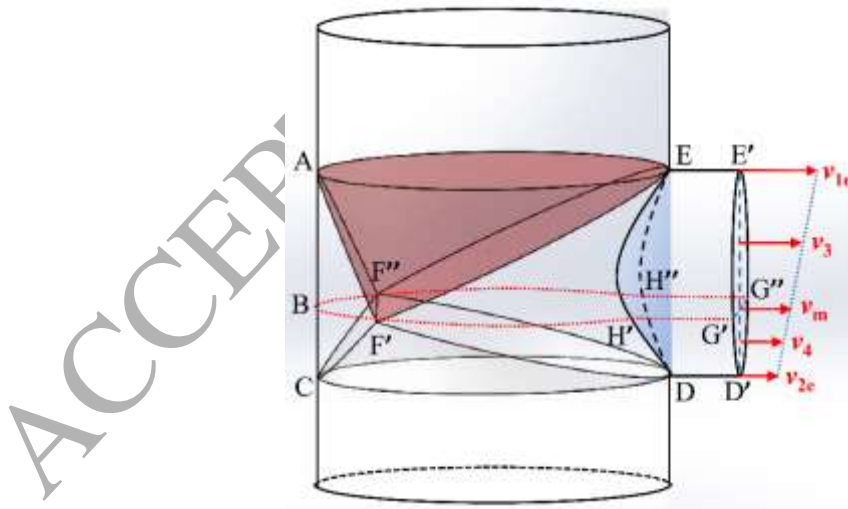


Fig. 2. The three dimensional model of velocity discontinuity and frictional surfaces in the DVSE process.

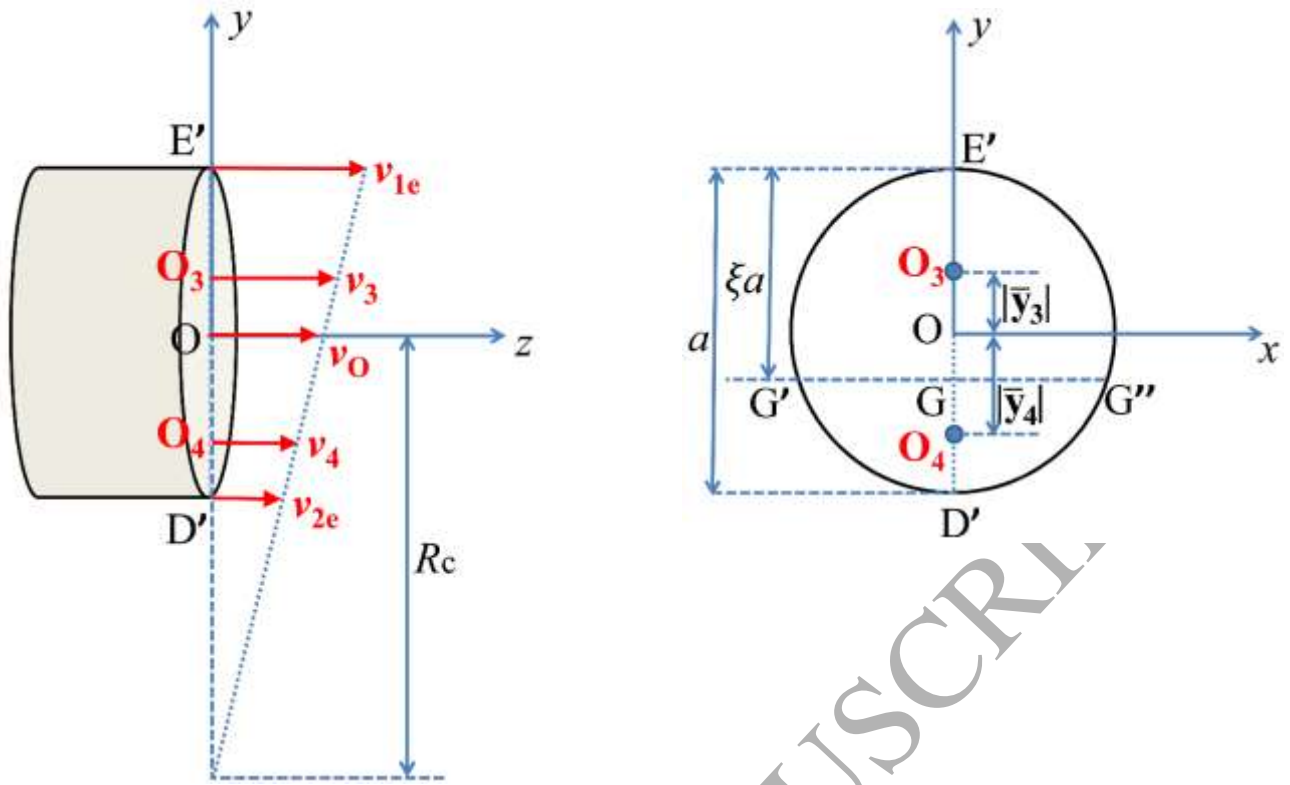
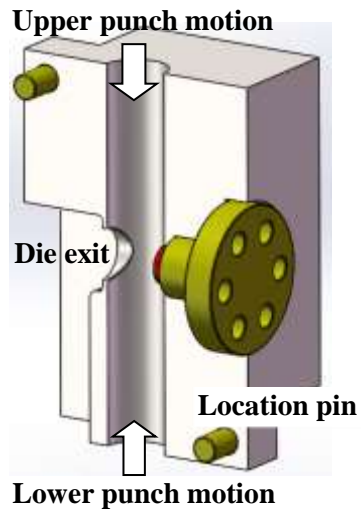
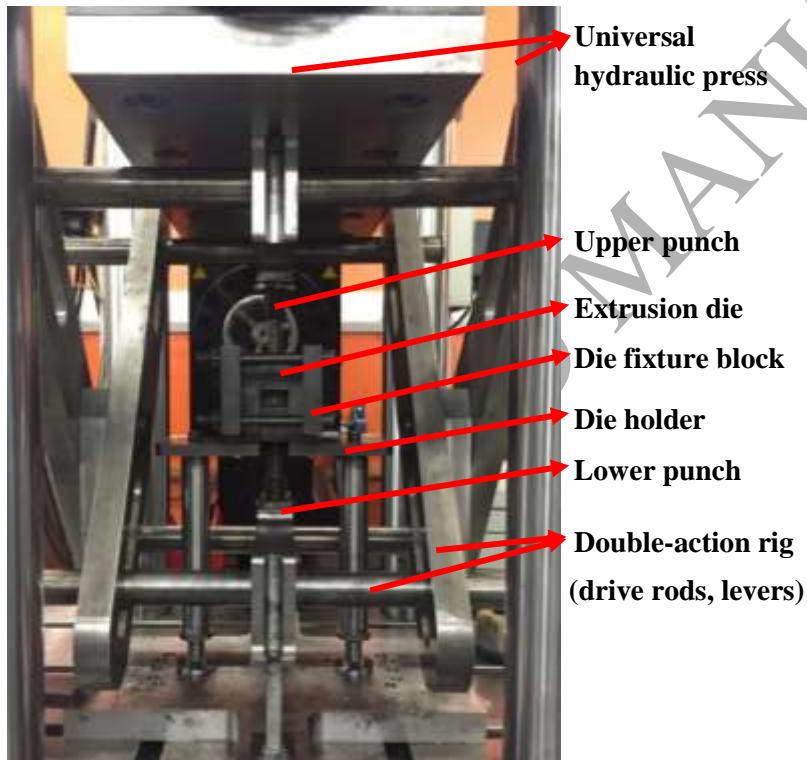


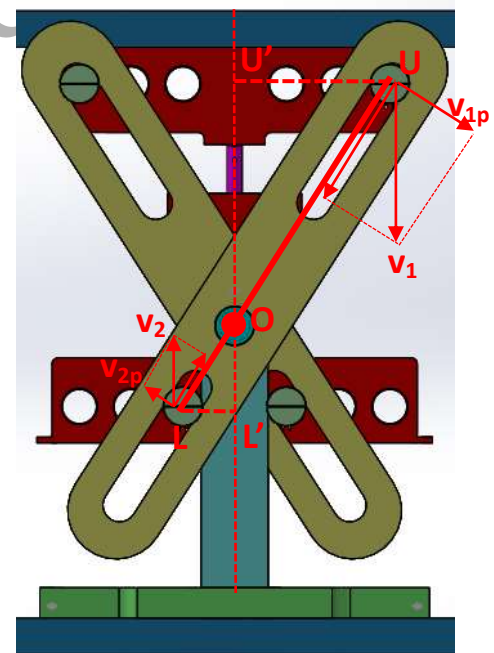
Fig. 3. The linear velocity distribution in the circular exit die and the bending curvature.



(a)



(b)



(c)

Fig. 4. (a) Designed and manufactured split extrusion dies, (b) extrusion die and double-action mechanism assembled on the 2500kN Instron universal hydraulic press, (c) illustration of the kinematics of the double-action mechanism [19].

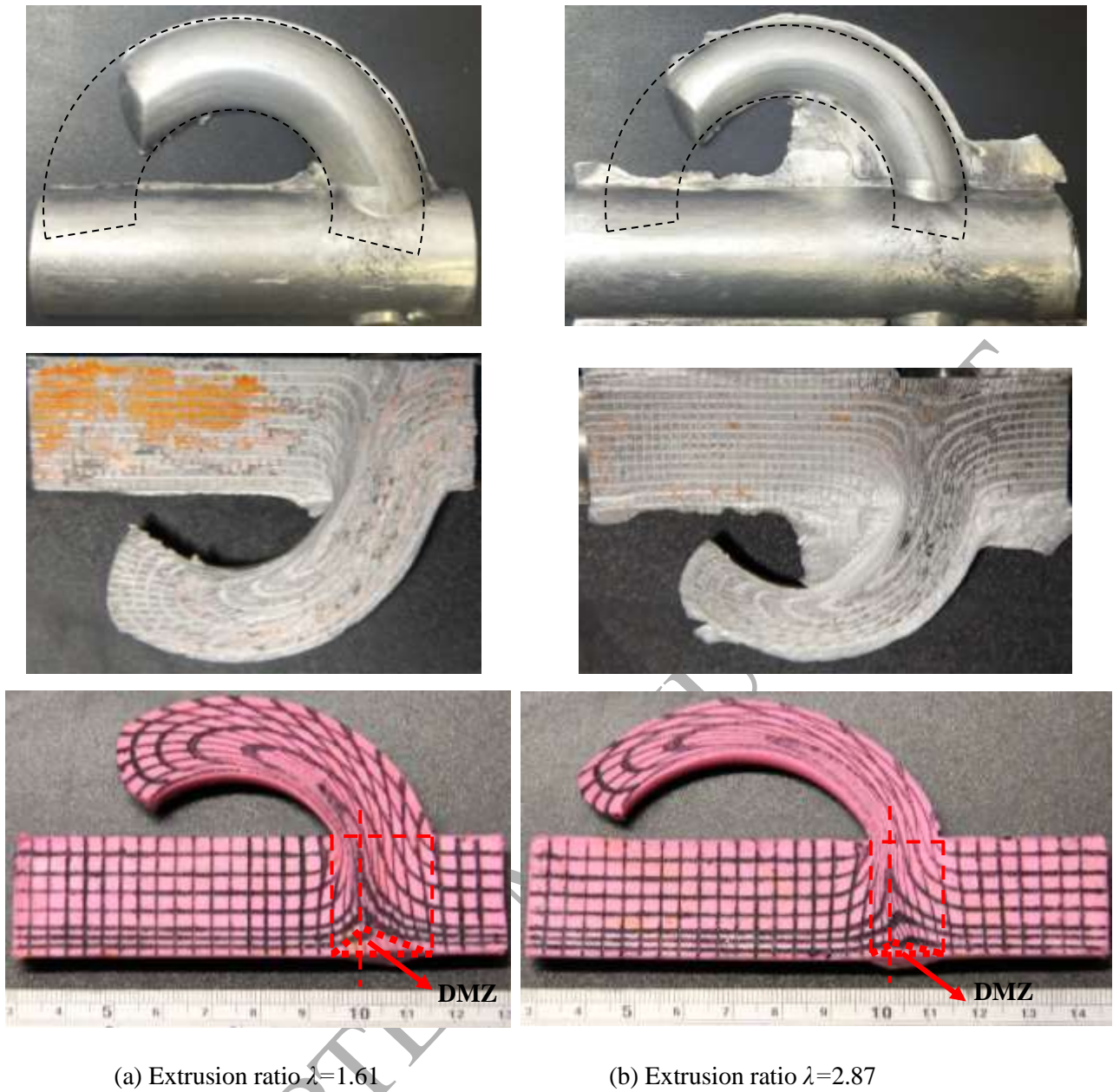


Fig. 5. Comparison of the curvature, grid distortion, and dead metal zone (DMZ) of extruded round bars obtained from the extrusion of AA1050 and model material plasticine at punch velocity ratio $v_2/v_1=0$ and extrusion ratios (a) $\lambda=1.61$ and (b) $\lambda=2.87$.

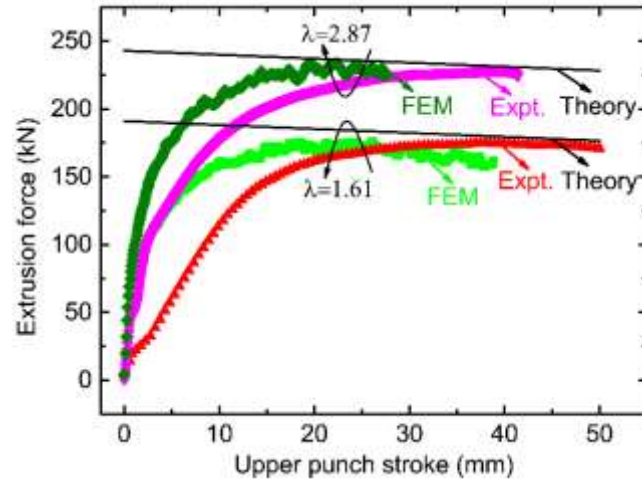


Fig. 6. Comparison of the load-displacement curve obtained from cold extrusion of AA1050, FE modelling and theory, at velocity ratio $v_2/v_1=0$ and extrusion ratios $\lambda=1.61, 2.87$, respectively.

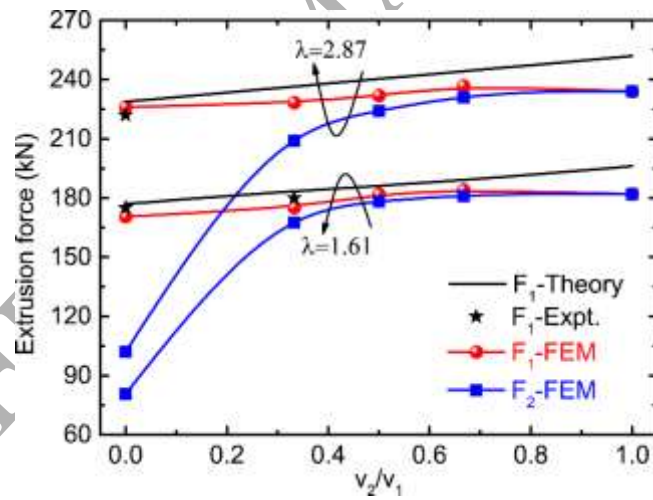


Fig. 7. Comparison of the extrusion force obtained from the extrusion of AA1050, FE modelling and theory, at velocity ratios $v_2/v_1=0\sim 1$ and extrusion ratios $\lambda=1.61, 2.87$, respectively

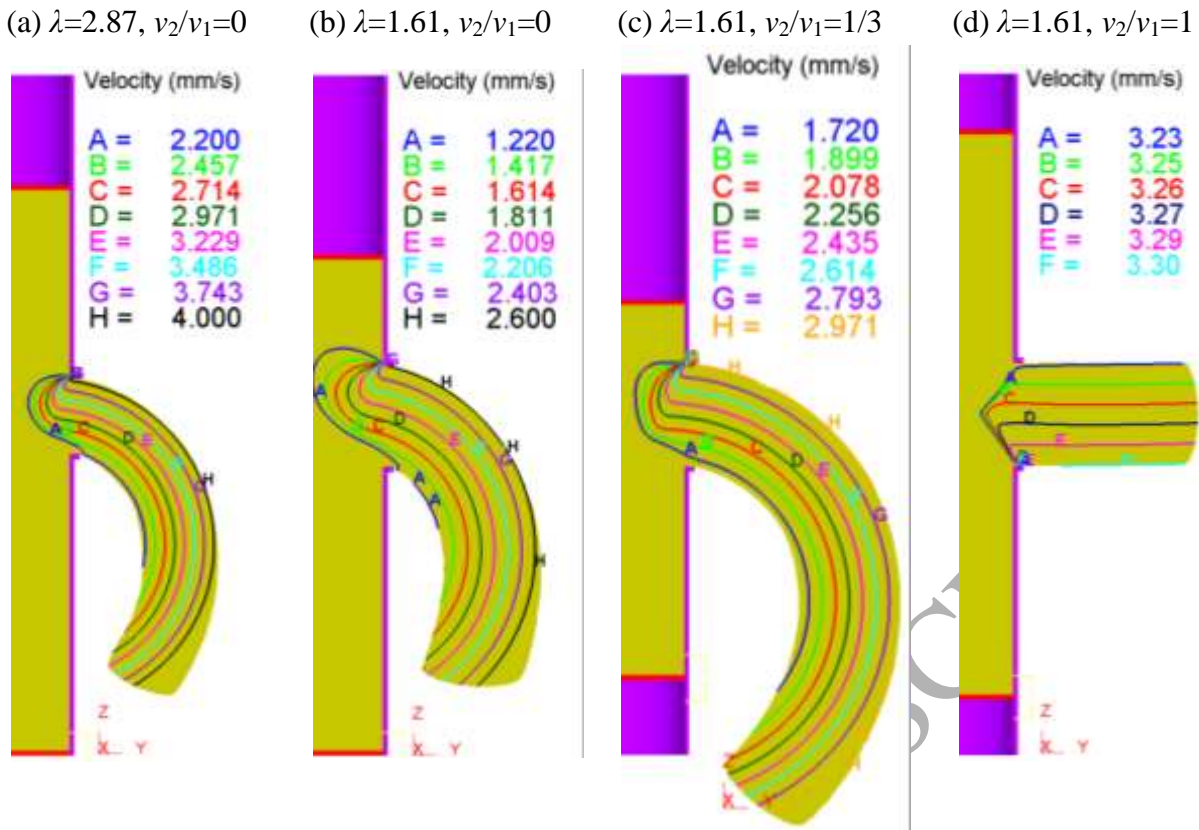


Fig. 8. Simulated material flow velocity distribution of the extruded round bars across the die exit.

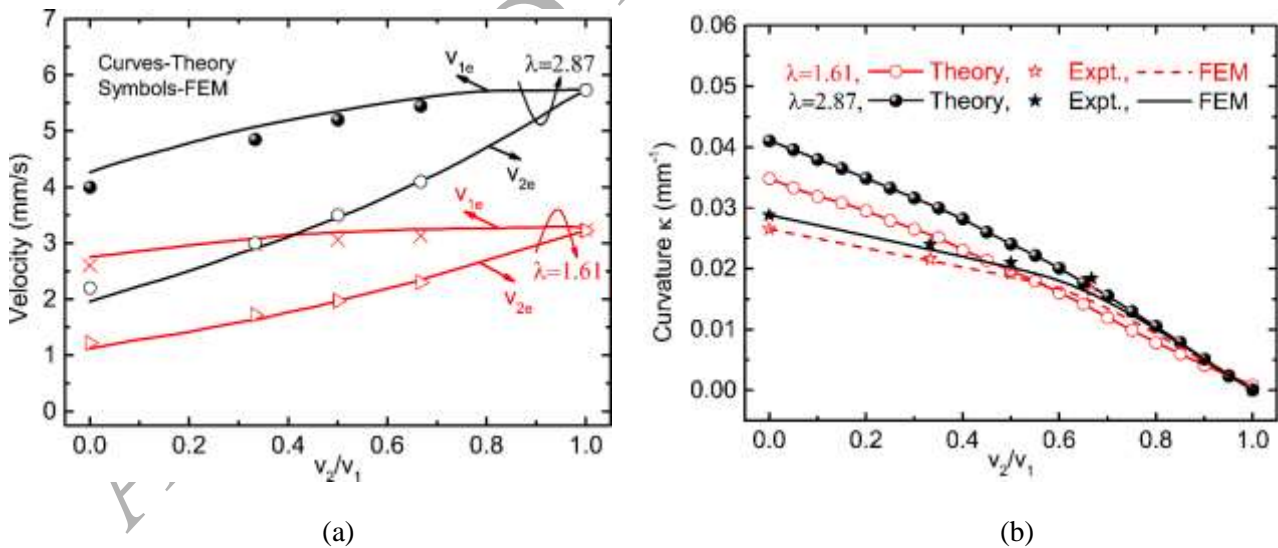


Fig. 9. Comparison of (a) the maximum and minimum material flow velocities across the die exit and (b) the curvature obtained from theory, FE modelling and plasticine extrusion experiments.

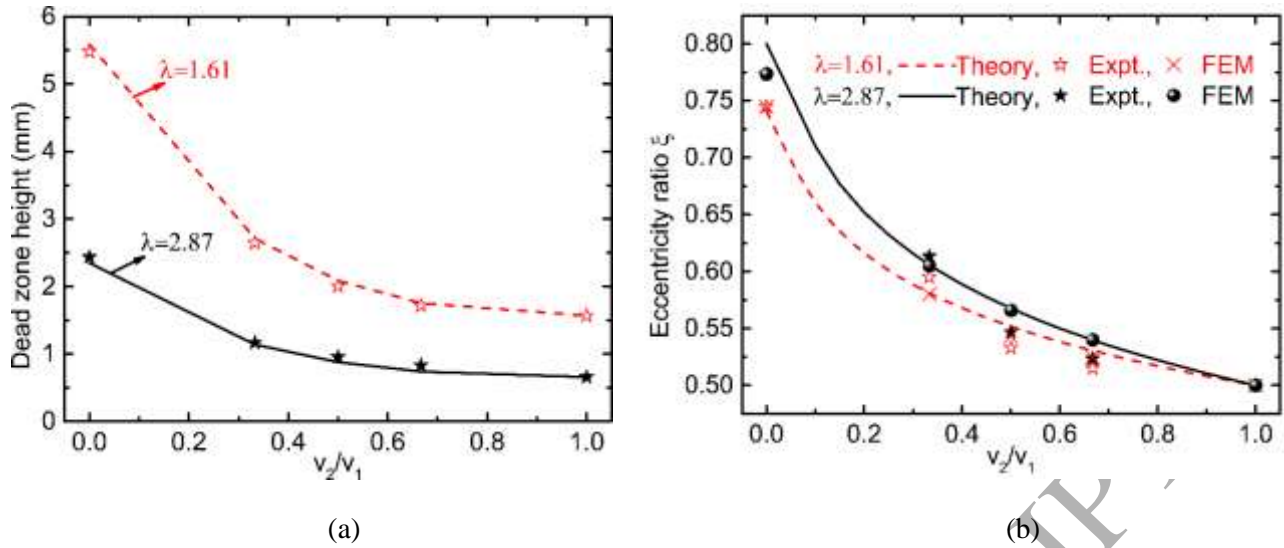


Fig. 10. Variation of (a) the dead zone height and (b) the eccentricity ratio ξ at velocity ratios $v_2/v_1=0\sim 1$ and extrusion ratios $\lambda=1.61, 2.87$, respectively.

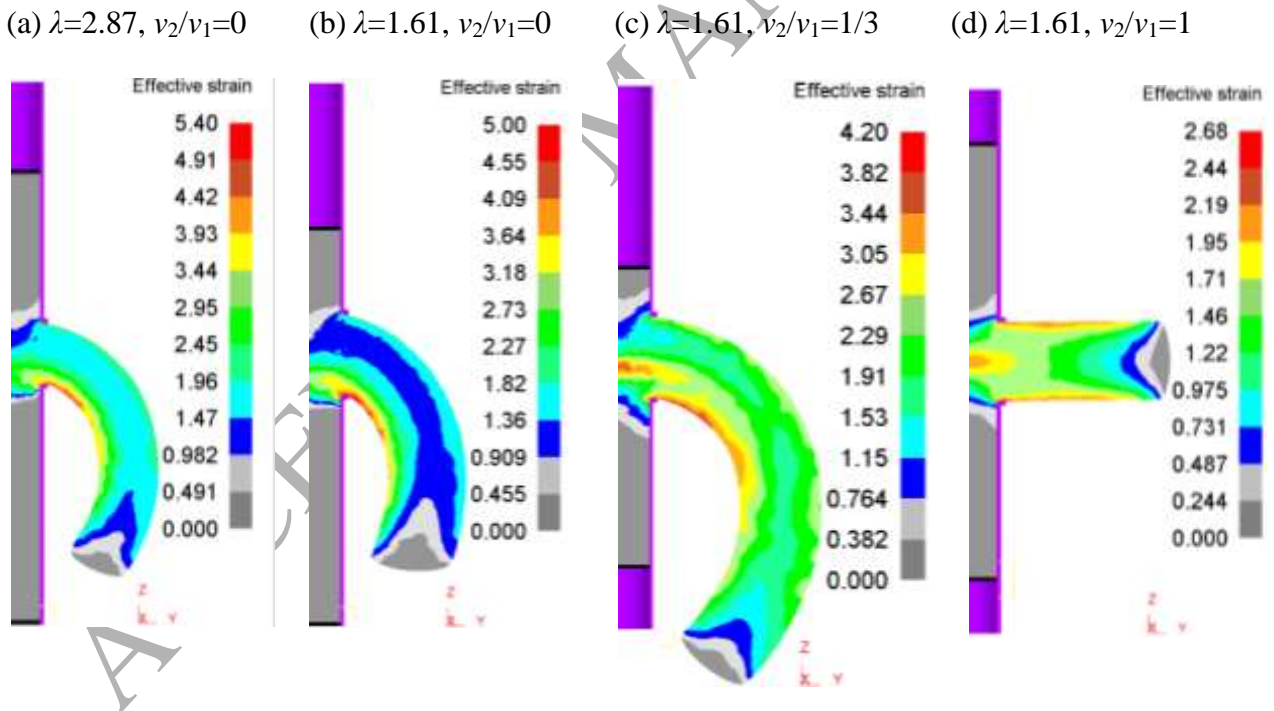


Fig. 11. Effective strain contours of extruded bars.

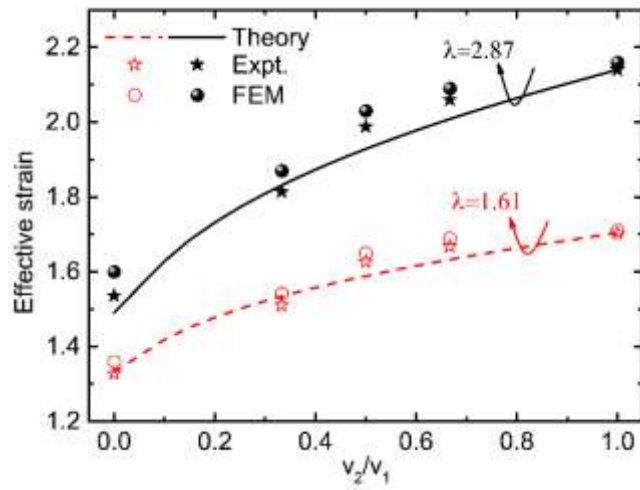


Fig. 12. Comparison of the effective strain of the outside bending region of the profile obtained from theory, FE modelling and plasticine extrusion experiments.

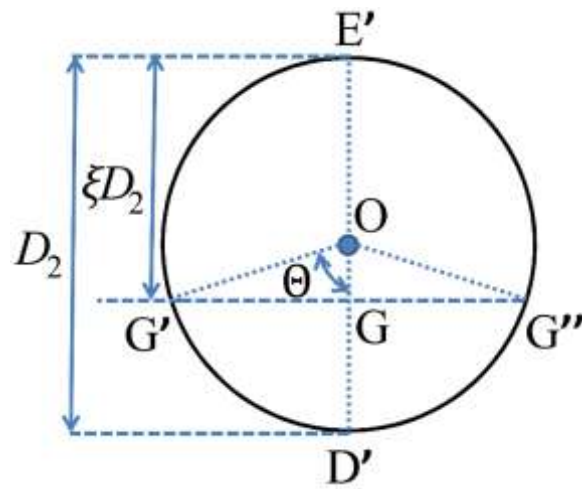


Fig. A1. Cross-section of the extruded profile or the die exit channel

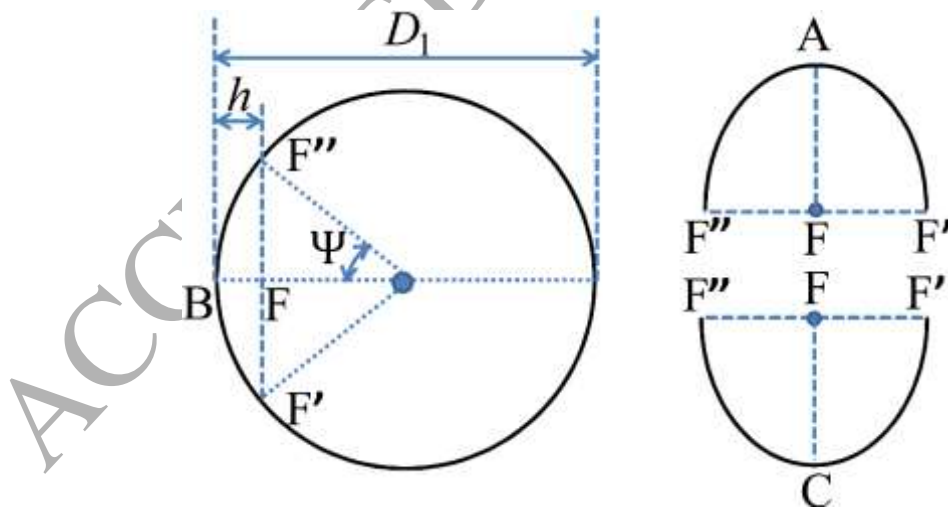


Fig. B1. The velocity discontinuity planes $AF'F''$ and $CF'F''$ of the DMZ boundaries

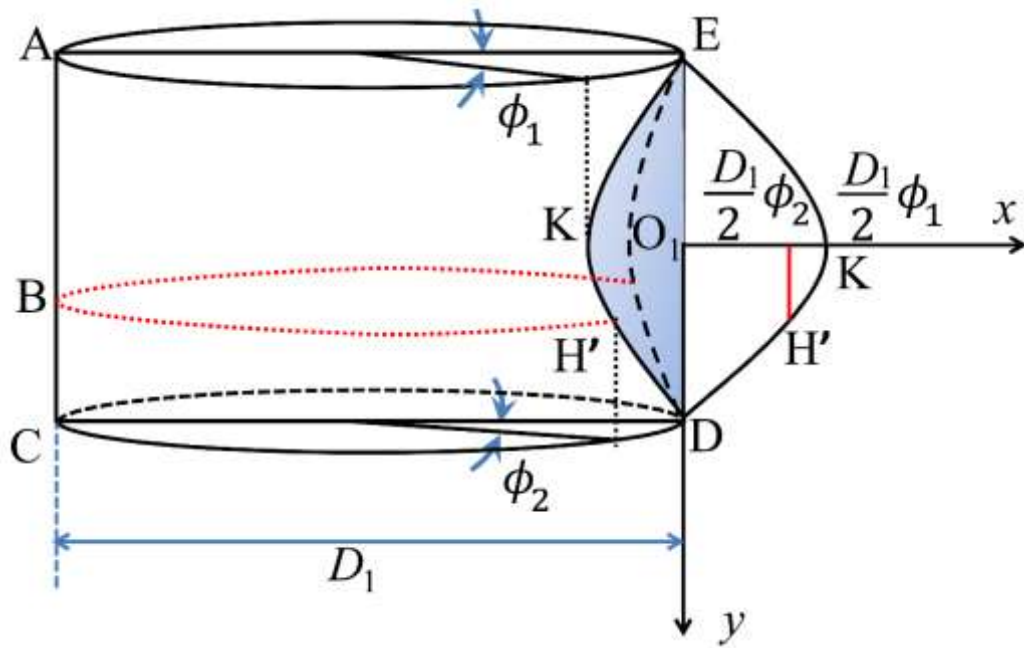


Fig. B2. The surface $EH'DH''E$ on the cylinder of diameter D_1 surrounded by the intersecting line of the two cylinders

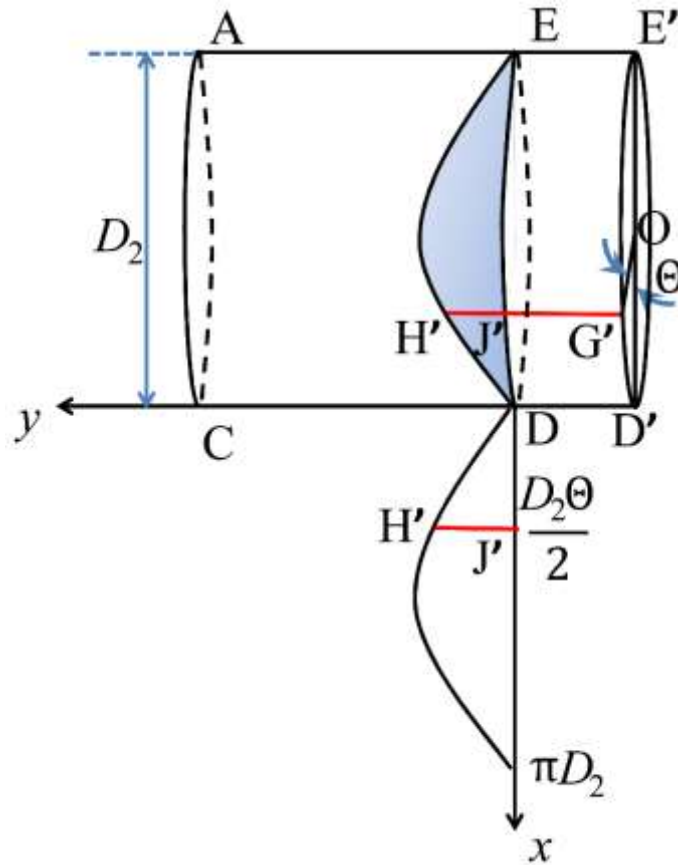


Fig. B3. The surface $EH'DJ'E$ on the cylinder of diameter D_2 surrounded by the intersecting line of the two cylinders

Graphical Abstract

